Modeling of brain efflux

Constraints of brain surfaces

Bork, Peter A. R.; Hauglund, Natalie L.; Mori, Yuki; Møllgård, Kjeld; Hjorth, Poul G; Nedergaard, Maiken

Published in:
PNAS

Link to article, DOI:
10.1073/pnas.2318444121

Publication date:
2024

Document Version
Publisher's PDF, also known as Version of record

PNAS RESEARCH ARTICLE | BIOPHYSICS AND COMPUTATIONAL BIOLOGY

Modeling of brain efflux: Constraints of brain surfaces

Peter A. R. Bork[a], Natalie L. Hauglund[a], Yuki Mori[a], Kjeld Møllgård[b], Poul G. Hjorth[c], and Maiken Nedergaard[a,1]

Edited by Terrence Sejnowski, Salk Institute for Biological Studies, La Jolla, CA; received October 23, 2023; accepted March 4, 2024

Fluid efflux from the brain plays an important role in solute waste clearance. Current experimental approaches provide little spatial information, and data collection is limited due to short duration or low frequency of sampling. One approach shows tracer efflux to be independent of molecular size, indicating bulk flow, yet also decelerating like simple membrane diffusion. In an apparent contradiction to this report, other studies point to tracer efflux acceleration. We here develop a one-dimensional advection–diffusion model to gain insight into brain efflux principles. The model is characterized by nine physiological constants and three efflux parameters for which we quantify prior uncertainty. Using Bayes' rule and the two efflux studies, we validate the model and calculate data-informed parameter distributions. The apparent contradictions in the efflux studies are resolved by brain surface boundaries being bottlenecks for efflux. To critically test the model, a custom MRI efflux assay measuring solute dispersion in tissue and release to cerebrospinal fluid was employed. The model passed the test with tissue bulk flow velocities in the range 60 to 190 µm/h. Dimensional analysis identified three principal determinants of efflux, highlighting brain surfaces as a restricting factor for metabolite solute clearance.

advection–diffusion | glymphatics | MRI

Significance

Fluid flows into and out of the brain have been studied for decades, but due to the technical challenges of imaging under the skull, classical empirical reports contain apparent contradictions and are inconclusive about whether the brain tissue itself has bulk flow through it. We here propose a simplified advection–diffusion-based model which highlights the critical role of surface membranes and resolve the apparent contradictions in the classical empirical reports. We then perform histological analyses to determine surface membrane parameters and record magnetic resonance images to test the model. The model is able to represent the data and indicates that advection contributes to steady-state waste clearance through a surface membrane bottleneck.

The rapid metabolism of the brain requires similarly rapid clearance of decayed proteins and metabolites to prevent waste accumulation. The sleep duration of mammals scales with their brain metabolism (1, 2), and sleep drives metabolite clearance while the brain's extracellular space is enlarged (3). The enlargement of the extracellular space during sleep may facilitate greater advection (bulk flow) of solutes out of the brain (4). However, whether bulk flow through tissue contributes to clearance is debated.

Two efflux assays provide the current state-of-the art efflux data but also pose two apparent contradictions (Fig. 1). In the classical efflux assay by Cserr et al. (5), radiolabeled tracers were infused into rat brains and their masses measured in whole brains harvested at 1, 4, 18, and 28 h after injection. Large and small tracers were found to clear from the brain with the same exponential decay rate, leading many to conclude that efflux was independent of molecular size and therefore primarily driven by bulk flow, rather than inherently size-dependent diffusion. However, in each case, the rate of efflux also decelerated in a very similar fashion to first-order transport kinetics, or simple diffusion across a membrane. The relative contribution of diffusion could not be determined from those early experiments. Replication studies by Groothuis et al. found the same single exponential decay but at a five times faster rate (6). The difference is likely due to choice of anesthetics, with ketamine-xylazine causing faster efflux than pentobarbital, but the pharmacological mechanism for this difference has not been clearly identified. The recent efflux assay by Pla et al. (7), which uses ketamine-xylazine anesthesia, sought to improve temporal resolution and the amount of data gathered per animal. Here, the tracer-molecule DB53 was infused in the mouse brain, and its concentration in the blood was quantified in each animal over the following 2 h (7). Since DB53 is trapped in blood by albumin, this measurement reflects total brain efflux by any route. The efflux accelerated throughout the observation period, in contrast to the slowing efflux observed when quantifying tracer efflux by harvesting the brains of multiple rats at increasing durations after tracer injection. To our knowledge, these two apparent contradictions in the experimental approach to determining brain efflux are so far unexplained.

Here, we seek to investigate whether the apparent contradictions can be resolved by modeling of brain solute transport as a combination of bulk flow and diffusion in a brain in which the surface membrane covering the brain acts as a barrier for export. This idea arose from the mathematical requirement that boundary conditions are specified for solving the transport differential equations. As we show below, such a surface layer would be a bottleneck for efflux which could explain the long-term slowing of efflux, while potentially allowing diffusion on the short time-scale to cause early acceleration of the tracer efflux concentration. Additionally, the difference between pentobarbital

Author affiliations: [a]Center for Translational Neuromedicine, Faculty of Health and Medical Sciences, University of Copenhagen, Copenhagen 2200 Denmark; [b]Department of Cellular and Molecular Medicine, Faculty of Health and Medical Sciences, University of Copenhagen, Copenhagen 2200 Denmark; and [c]Department of Applied Mathematics and Computer Science, Technical University of Denmark, Lyngby 2800 Denmark

Author contributions: P.A.R.B., K.M., and M.N. designed research; P.A.R.B., N.L.H., Y.M., K.M., and P.G.H. performed research; P.A.R.B., N.L.H., Y.M., K.M., and M.N. analyzed data; and P.A.R.B. and M.N. wrote the paper.

The authors declare no competing interest.

This article is a PNAS Direct Submission.

[1]To whom correspondence may be addressed. Email: nedergaard@sund.ku.dk.

This article contains supporting information online at https://www.pnas.org/lookup/suppl/doi:10.1073/pnas.2318444121/-/DCSupplemental.

Published April 10, 2024.

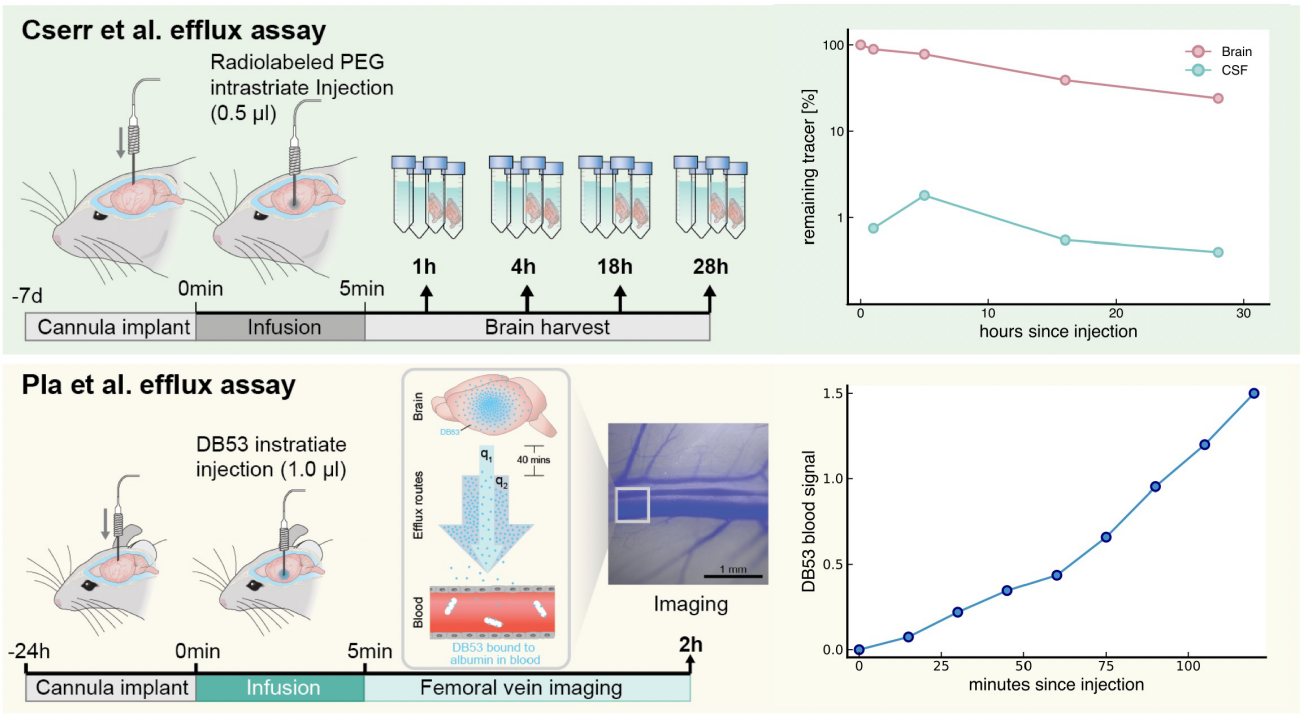

Fig. 1. Overview over previously published brain efflux assays used here. Two published tracer efflux assays by Cserr et al. (5) (*Top* row) and Pla et al. (7) (*Middle* row) provide the inspiration and validation for the one-dimensional model proposed here. Cserr et al. infused radiolabeled tracers into rat brains and measured tracer mass in cerebrospinal fluid (CSF) and whole brains harvested at 1, 4, 18, and 28 h (5). Large and small tracers were found to clear the brain at the same rate, indicating bulk flow efflux, but the rate decelerated over time, pointing to diffusive efflux. Pla et al. infused DB53 (0.96 kDa) in the mouse brain and quantified its accelerating concentration using fluorescence enhancement in the blood over the next 2 h, where it is trapped independent of efflux route by its strong binding with albumin (7).

and ketamine-xylazine anesthesia may reflect differential effects on the surface layer permeability. After validating that this model can represent the classical efflux data reported by Cserr et al. as well as the newer efflux data by Pla et al., we develop a custom in vivo efflux assay that provides the necessary spatial and temporal resolution to critically test the importance of brain surfaces in solute clearance. We finally extend the model to include endogenous waste production and the fundamental criteria for effective clearance. Based on the combination of data and quantitative modeling, bulk flow likely contributes to brain clearance and brain surface membranes likely play a previously unrecognized role in restricting solute clearance.

1. Mathematical Method: A Global Model of Brain Net Molecular Transport

We aim to construct a simple mathematical representation of fluid transport through the brain, its main cerebrospinal fluid compartments, and the blood, in order to account for the spread of endogenous and tracer molecules. Inspired by volume averaging techniques (8), we assume the tissue to be an unconsolidated homogeneous porous medium with diffusion and Darcy flow of solutes. Thinking first of the brain as a ball with ventricles in the center, we limited the average advection to the radial axis, orthogonal to the brain surface, and assumed spherical symmetry (Fig. 2*A*). Simplifying even further, we unfold the ball and model the brain as a simple slab in order to better capture the relatively large ventricular surface area compared to superficial surface area (Fig. 2*B*). These simplifications sacrifice realism of the spatially and temporally varying fluid field and reduces the model relevance to a time-scale of at least minutes (beyond relevant oscillations and pumping) and a length scale of at least tens of microns (beyond the resolution of perivascular spaces for example). The point is not to investigate tissue anatomy, but the net transport of molecules in particular across the brain surface, and our one-dimensional model represents the essential feature of depth between surfaces as well as both diffusive and bulk flow transport.

Since tracers move faster in cerebrospinal fluid than in tissue (21), we reasoned that as an approximation, we can assume rapid mixing in control volumes representing the ventricles and the subarachnoid spaces, on either side of the tissue slab. We therefore parameterized a boundary consisting of interaction with cerebrospinal fluid through a narrow membrane with diffusion D_m. The presumed single-cell layer is narrow (length L_m), and we can assume the concentration profile to reach steady state rapidly here and enforce conservation of mass in the net flux. Though conceived as a diffusivity, the D_m parameter is rather an effective permeability parameter of the surface membrane including effects of both pore space and transmembrane pathways.

We parameterize transport across the blood–brain barrier as well as endogenous production using reaction terms, as has been done before (8). With this extension, we can investigate the role of advection and diffusion for endogenously produced waste products. We also couple the subarachnoid space to the blood compartment using simple first-order kinetics. This disregards details of whether the transport outside the brain parenchyma goes directly into veins or indirectly via the lymphatic vessel but gives a parsimonious description of parenchyma efflux.

The resulting mathematical model (Eqs. **2**–**5**) depends on 12 parameters of which nine have been measured with reasonable reliability (Table 1). We therefore quantify our uncertainty on the remaining three parameters to complete the model. The effective diffusion parameter is uncertain but has a strong prior

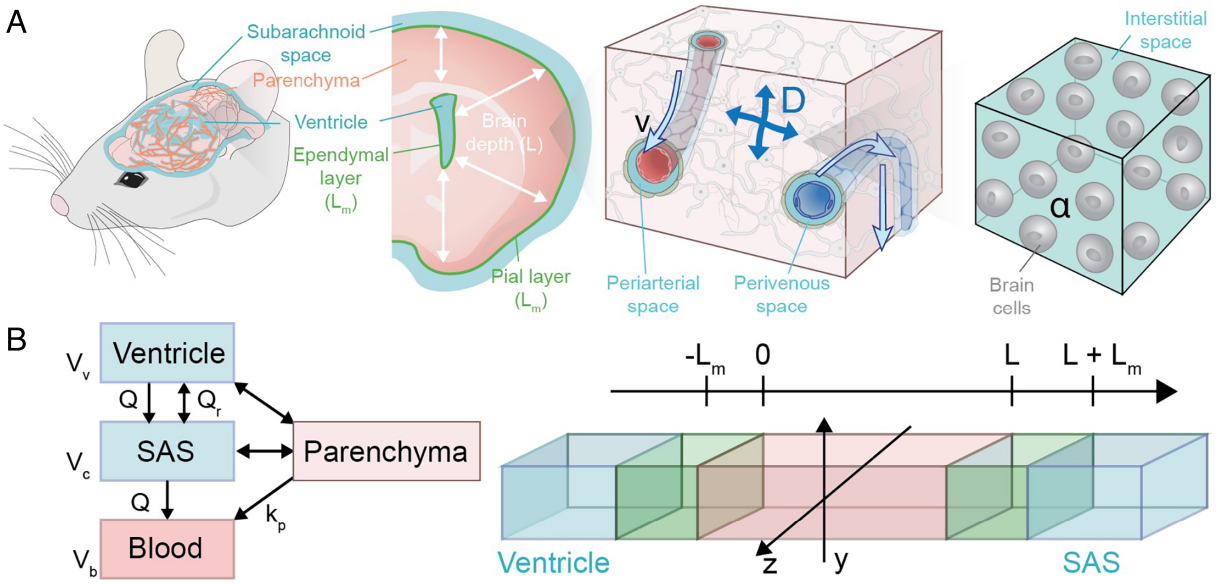

Fig. 2. One-dimensional and lumped advection–diffusion model of global brain solute transport. (*A*) In the murine brain, fluid flow is proposed along coronal radii (white arrows), with flow (light blue arrows) along vasculature and interstitial diffusion (cross-arrow) in the extracellular space (teal). Molecular concentrations and transport are averaged over small tissue volumes (cubes) which are taken to be homogeneous porous media with tortuous diffusion (8) and Darcy flow. Bulk flow along vasculature (blue arrows) is taken to primarily run between ventricles and the subarachnoid space surface in the coronal section (white arrows), where solutes mix rapidly and are transported to blood. (*B*) This biology is reduced to three control volumes representing ventricles, subarachnoid space (SAS), and blood and a one-dimensional advection–diffusion–reaction model, oriented along the average bulk flow directions. From tissue parenchyma (pink), molecules diffuse over surface membranes (green, not to scale) to either ventricles or subarachnoid space compartments, each with rapidly mixing cerebrospinal fluid, and are then taken to blood with first-order mass transport kinetics. Endogenous production and transport across the blood–brain barrier is evenly distributed in the tissue (as reaction terms; see Eqs. **2**–**5**). Constants and parameter descriptions are listed in Table 1.

from empirical work (22) and recent advanced modeling with precise human geometries indicate that it is constant across the brain (23). Advection in the tissue has not been measured, so we put a normal prior on this parameter centered on zero. Finally, the diffusion through surface membranes has very little prior knowledge, and we assign a uniform prior from zero to the expected tissue diffusion. Via Bayes' theorem, we can then approximate the posterior (here: data-informed) probability distributions for the uncertain parameters.

To summarize, our model of global brain molecular transport is a probabilistic one-dimensional advection–diffusion–reaction equation with boundaries to ventricular and subarachnoid space cerebrospinal fluid and blood compartments (Fig. 2 and Eqs. **2**–**5**). When coupled with data observation models, we can update our priors in light of data and estimate the full data-informed probability distributions of our uncertain parameters and evaluate whether the model validly represents these datasets with those parameters.

Table 1. Model parameters

Description	Symbol	Mouse	Rat
ECS volume fraction [0 − 1]	α	0.2 (3)	0.2 (9)
Brain depth [mm]	L	2.0 (10)	3.0 (11)
Surface area [mm^2]	S	52 (12)	142 (12)
Surface layer depth [mm]	L_m	0.01 (13), Fig. 5	0.01 (13), Fig. 5
BBB efflux (Cserr) [h^{-1}]	k_p	0 (14)	0 (14), [0.432 (5)]
CSF volume [mm^3]	V_c	36 (15)	370 (15)
Blood volume [mm^3]	V_b	1490 (16)	10,200 (17, 18)
SAS efflux [mm^2h^{-1}]	Q_l	20 (19)	200*
Ventricle reflux [mm^2h^{-1}]	Q_r	3.6 (20)	36*
Average velocity [$mm\,h^{-1}$]	v	0.0	0.0
Membrane diffusion [mm^2h^{-1}]	D_m	0.25	0.25
Effective diffusion [mm^2h^{-1}]	D	0.46 (9)	0.46 (9)

Of the 12 parameters required for the model, eight were determined from the literature, one was determined from our histology (L_m), and three were considered uncertain (v, D_m, and D). The table lists our prior expected values in boldface for the uncertain parameters (*Materials and Methods*), while our data-informed estimates are in Figs. 3 and 4. A * indicates the cerebrospinal fluid flow rates for the rat were scaled from the mouse data by the ratio of their cerebrospinal fluid volumes.

2. Results

2.1. The Global Brain Solute Transport Model Fits the Two In Vivo Efflux Assays. To test the validity of the model for global efflux from the brain we first implemented an analysis of the classical efflux study in the Cserr dataset (5). In this study, radiolabeled tracers of 0.9, 4, and 69 kDa were injected into rat brains, and masses measured in the entire brain and cerebrospinal fluid four times over the following 30 h (5). The model posterior predictions are all close to the data (Fig. 3 *B* and *C* and *SI Appendix*, Fig. S1 and Movies S1–S3). Cerebrospinal fluid concentrations are slightly overestimated at 15 h post injection, but otherwise very close to the prediction mean. The model may underestimate cerebrospinal fluid clearance in this case, since the discrepancy is larger at the late time points but in better agreement earlier on when transport from the brain is more important. For each tracer, the estimated effective diffusion coefficient stayed close to its own strong prior, whereas estimates of membrane permeability and velocity overlapped between the tracers (*SI Appendix*, Fig. S1). In spite of minor discrepancies, the model fits

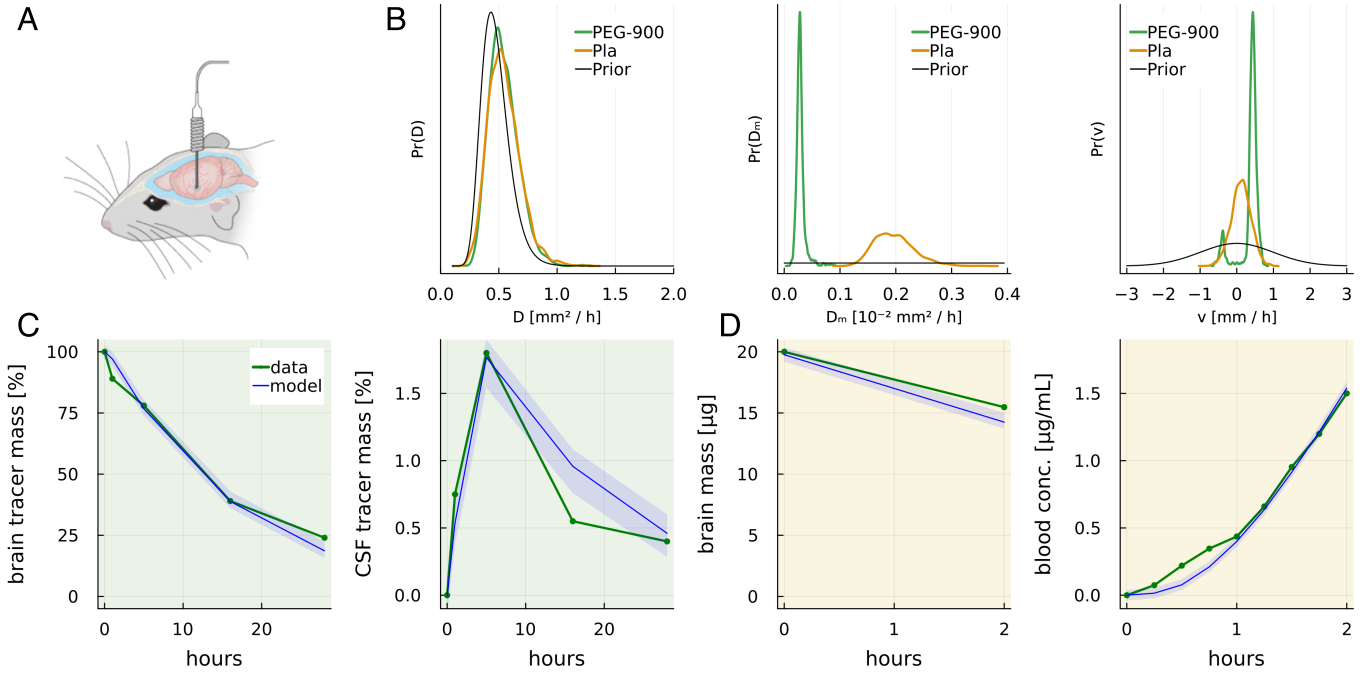

Fig. 3. Data-informed parameter distributions and model predictions agree with both rat and mouse in vivo efflux datasets. (*A*) Both efflux datasets rely on intrastriatal injections. (*B*) There is considerable overlap on data-informed probability distributions for the effective diffusion parameter D in the Cserr and Pla datasets with prior knowledge based on diffusion assays (9) (shown here is Cserr's PEG-900 tracer, see *SI Appendix*, Fig. SI 1 for PEG-4000 and albumin). Based on the Cserr efflux study, surface membrane permeability D_m estimates are smaller than in the Pla dataset and the model is unable to distinguish the direction of bulk flow, but prefers a speed of 0.3 mm/h. The data-informed probability distribution for bulk flow based on the Pla study overlaps zero, with 95% of the probability mass between −0.47 mm/h and 0.83 mm/h. Compared to the prior (black, shown on restricted interval) the data-informed distributions are more precise. (*C*) There is considerable overlap with the longer duration efflux data on remaining tracer mass in rat brain and cerebrospinal fluid (CSF) from the Cserr study. (*D*) Mouse total brain content and blood concentrations from the Pla et al. study agree with data-informed model predictions. Blue lines: mean posterior prediction, blue shadow: one SD from mean.

these datasets of total brain efflux and cerebrospinal fluid content of tracers in the 30 h following intrastriatal infusion in rats. This is particularly interesting because the model here concurs with the observation by Cserr et al. that at this long time-scale, efflux essentially reduces to a single exponential decay rate, in spite of its spatial organization and large variations in molecular size.

At a much shorter time-scale but with an approach that allows kinetic analysis in individual mice, the recent Pla dataset investigated efflux of DB53 (0.96 kDa) from intrastriatal infusion to the blood. This dataset includes tracer distribution shortly after infusion, providing us with good initial conditions for efflux modeling. The authors here found the tracer concentration in the blood to accelerate at early times, contradicting the single exponential decay rate found by Cserr for longer time-scales, in spite of the tracers being of the same size (Fig. 3*D* and Movie S4). The model predictions agree with the measured blood concentrations and brain tracer mass measurements. The largest discrepancy is in the earliest phase, where experimental tracer arrives earlier in the blood than in the model, something which could be due to a slightly too narrow initial spread or underestimated transport in cerebrospinal fluid.

The discrepancies between model prediction and data are therefore small and the model captures both the single decay rate over long times found by Cserr et al. and the accelerating efflux at early times found by Pla et al. The apparent contradiction between these two datasets is resolved by the surface membrane boundary conditions: As is especially evident in Movies S1–S3, tracers diffuse within the brain faster than across the surface membranes. The lack of overlap in the data-informed probability distributions for surface diffusivity, D_m, may be due to the differential effects of ketamine-xylazine versus pentobarbital anesthesia, where the latter leads to a more restrictive membrane in the Cserr datasets (*SI Appendix*, Fig. S1).

Since an extensive experimental literature quantifies effective diffusion on tracers in the brain, we have prior data about our parameter D and our posterior estimates should therefore stay on this prior (see e.g. refs. 8, 9, 22). This is doubly so since large and small tracers are indistinguishable in the data. For each of the datasets, we calculated the Stokes–Einstein diffusion and used the corrections for extracellular space volume fraction and interstitial tortuosity found by Nicholson et al. (8, 22), including measurement variance, to set our expected D (*Materials and Methods*). The prior effective diffusion distribution is close to the posterior distributions for each of the tracers used by Cserr (*SI Appendix*, Fig. S1). This confirms that our model concurs with the large literature on interstitial diffusion measurements.

2.2. Either Bulk Flow or Open Surfaces Are Required for Efflux in the Efflux Assays without Spatial Resolution. In view of the agreement between data and data-informed model predictions as well as prior and data-informed diffusion parameter estimates, we can next evaluate the entire data-informed probability distribution for the surface membrane (D_m) and bulk flow parameters (v). The surface membrane diffusivity D_m is estimated to be much smaller than the interstitial diffusivity D in especially the Cserr data but also in the Pla data. The bulk flow speed with maximum data-informed probability is 0.3 mm/h in the Cserr data though the direction cannot be inferred. In the Pla data bulk flow cannot be identified, with 95% of the probability mass being between −0.32 mm/h and 0.54 mm/h. The joint probability distribution between bulk flow and surface diffusivity indicates

that slower bulk flow requires faster surface transport in order to fit the data (*SI Appendix*, Fig. S2).

2.3. Validation with Real-Time In Vivo MRI. The uncertainty remaining in the data-informed parameter estimates is likely due to the lack of spatial resolution in the efflux assays. We therefore adapted the efflux assay by Pla et al. and the fast dynamic contrast-enhanced MRI developed by Stanton et al. (21) to improve spatiotemporal resolution. Briefly, gadobutrol (0.6 kDa) was infused in mouse striatum under ketamine-dexmedetomidine anesthesia and frames were captured every 6 min (*Materials and Methods*). By quantifying tracer concentration along a straight line in the coronal section, we generated spatiotemporal measurements corresponding to the tissue model (Fig. 4*A*). This setup let us image blood–brain barrier-constrained tracer through the mostly closed skull (14).

The data-informed model predictions align with the measurements (representative example in 4 *B*–*G*, each recording in *SI Appendix*, Figs. S3–S9 and Movie S5). In the ventricles, where dependence on parameter values is large, the predictions undershoot the measurements. Still, qualitatively and quantitatively, the measured concentrations within the brain agree with the data-informed predictions (Fig. 4 *C*–*G*). Additionally, the data-informed distribution on effective diffusion concurs with our strong prior knowledge (Fig. 4*B*). We performed parameter robustness analyses for each recording by replacing each physiological constant with a normal prior before parameter estimation and found no substantial differences though improved fits to data (*Materials and Methods* and *SI Appendix* electronic materials). In sum, the model is able to represent the tracer evolution in this custom efflux assay.

Based on the measurements of tracer kinetics inside the closed skull, the surface membrane diffusion and bulk flow parameters now have more precise data-informed probability distributions (Fig. 4*B*). The surface permeability is estimated in the same range, but a bit greater than the estimate based on the Pla dataset, and there is approximately no interaction with bulk flow (*SI Appendix*, Fig. S10). The surface membranes are therefore also an efflux bottle-neck in this case. The data-informed bulk flow estimate is within the broad range from the Pla-based estimates but here rejects zero advection since all of the sampled probability mass reflects proper flow.

2.4. Boundaries Consist of Multiple Differentially Organized Cell Layers. The microscale boundaries are beyond MRI resolution for in vivo imaging, but with histological methods, we can map the territories neighboring the ventricles and subarachnoid spaces. The model averages out the specific transport character-

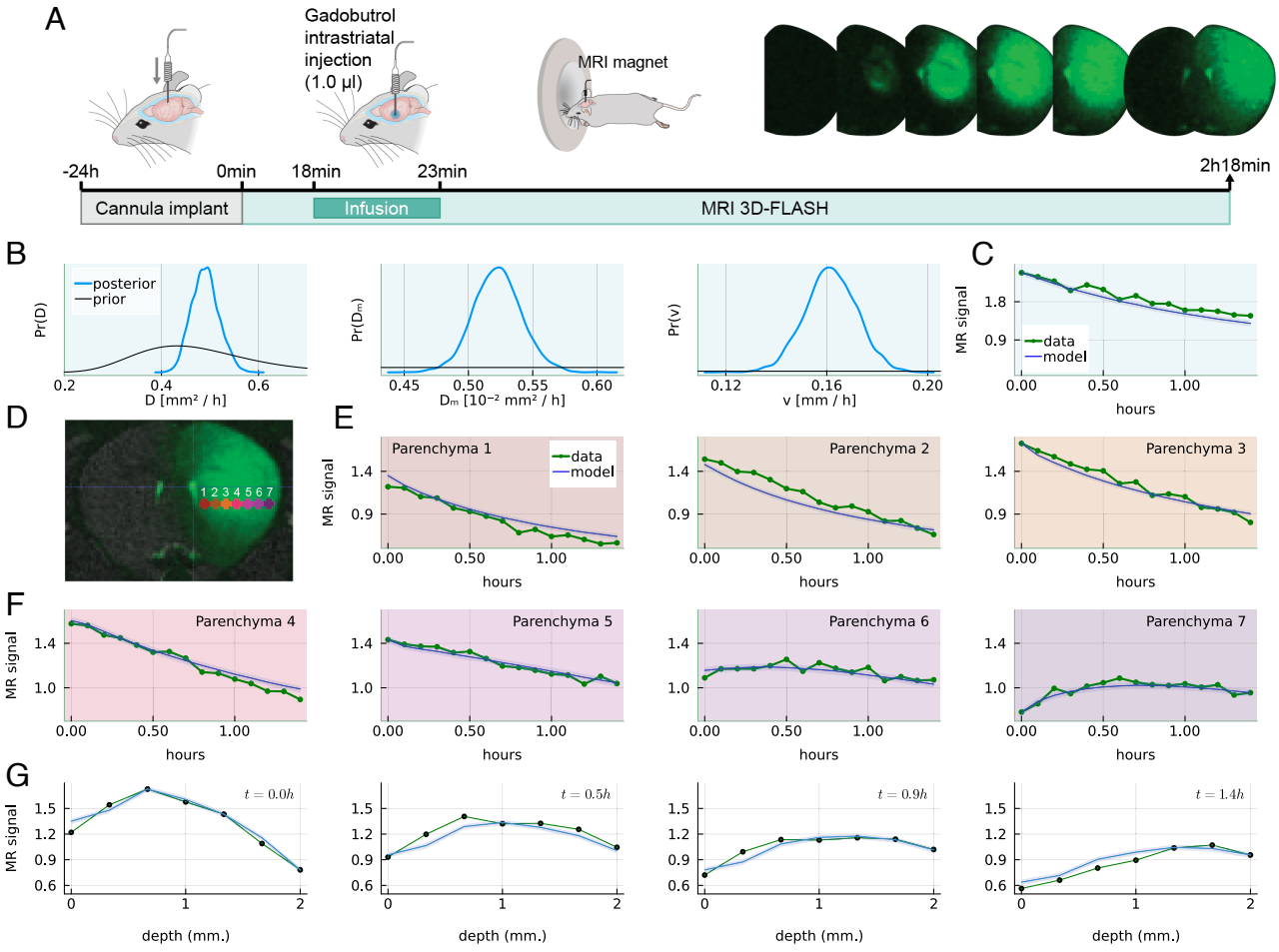

Fig. 4. Real-time in vivo solute kinetic measurements in the closed skull. (*A*) In this custom efflux assay, we infused gadobutrol (0.6 kDa) in mouse striatum and measured tracer concentration in seven regions of interest on the coronal plane. Representative stills taken during the 2 h after tracer infusion with regions of interest illustrated. (*B*) The posterior effective diffusion coefficient aligns with priors. The membrane diffusion coefficient is similar to estimates based on the Cserr and Pla datasets. The estimated velocity component is small but nonzero with maximum probability of 0.16 mm/h. Due to information in the data, the data-informed distributions for D_m and v are each narrow on a small interval under the prior (in black, shown partly). (*C*–*G*) The model data-informed predictions (blue) fit the custom MR measurements of tracer at seven regions of interest (*D*) after intrastriatal infusion seen across time (*E* and *F*) and over the brain depth (*G*) (representative example, see each recording in *SI Appendix*, Figs. S3–S9).

istics of these important zones, so to clarify the interpretation of the model, we require a clear picture of their anatomy. In Fig. 5, we show a coronal section of a mouse brain in the same plane as those imaged with MRI, but stained with markers of glial cells and aquaporins. At the macroscopic scale, panel b shows gaps corresponding to vessels oriented along the modeled axis in the cortex, corresponding to our hypothesis that transport primarily occurs along this axis in the cortex. On the ependymal (inner) surface, a single-cell layer is visible after staining with Aquaporin-4 (AQP4) (Fig. 5*C*). Staining with Glial Fibrillary Acidic Protein (GFAP) reveals the extensive stem cell niche of the anterior horn (Fig. 5*C*). On the outer surface (glia limitans) a much thicker zone is strongly positively stained for AQP4 and to a lesser degree GFAP (Fig. 5*D*) (24). The glial endfeet layer at the outer surfaces shows a marked GFAP staining. These molecular differences between inner and outer surfaces are likely to have different consequences for transport, something which will require advances in imaging resolution to investigate in vivo.

The model presented here takes the primary bottleneck for large scale transport from the brain to ventricles to be a 10 μm layer of interweaved GFAP and AQP4 expressing astrocyte processes (24, 25), corresponding to our choice of the L_m parameter (see Fig. 5*C*, green arrowheads and bar and Table 1). The large subependymal zone, which houses stem cells and likely severely controls transport, covers a sizeable fraction of the ependyma (Fig. 5*C*). (While our model reflects this using the parameter r_e, see methods, this ratio cannot be determined within MRI resolution but should be a future experimental target). It has recently been reported that a specialized subtype of astrocytes cover the glia limitans superficialis in a layer 0.01 to 0.03 mm thick, with unclear coverage of the ventricles (26). For the purpose of minimalist modeling, we have found that averaging over inner and outer surfaces provides a sufficient description of concentration of our small inert tracer, but this should not be taken to indicate that the boundaries are similar with respect to other transport processes.

2.5. Bulk Flow and Surface Openness Both Substantially Reduce Endogenous Brain Waste in the Stable State. Since the ultimate purpose of these investigations is to understand the fundamental aspects of global molecular clearance of metabolites, we extended the model to include endogenous waste solutes by using a production rate p as has been done before (8) and performed a dimensional analysis (*Materials and Methods*). A main advantage of a nondimensionalized model is that the results can be extrapolated, as long as the nondimensional parameter groups are scaled accordingly. When waste is rapidly cleared from the cerebrospinal fluid and blood, the model can be reduced to three (nondimensional) parameters. One is the Péclet number, which is the ratio of bulk flow to diffusive transport over the length of the brain, $\mathrm{Pe} = \frac{vL}{D}$. Another is the relative surface membrane transport, specifically the ratio of diffusive flux across the surface membrane to that within the brain, $\gamma = \alpha \frac{D_m}{L_m} / \frac{D}{L}$ (adjusted for extracellular space volume fraction α). The last is the relative clearance over the blood–brain barrier compared to interstitial diffusion, $\phi = k_p L^2 / D$. Being mostly interested in the case when the clearance across the blood–brain barrier is low, we continue our analysis with $\phi = 0.1$ (other choices yield similar results). The total brain content of endogenously produced waste in the steady state is now a function of the Péclet number and the relative surface membrane transport γ, see Fig. 6. Both make significant contributions to waste clearance, in this model.

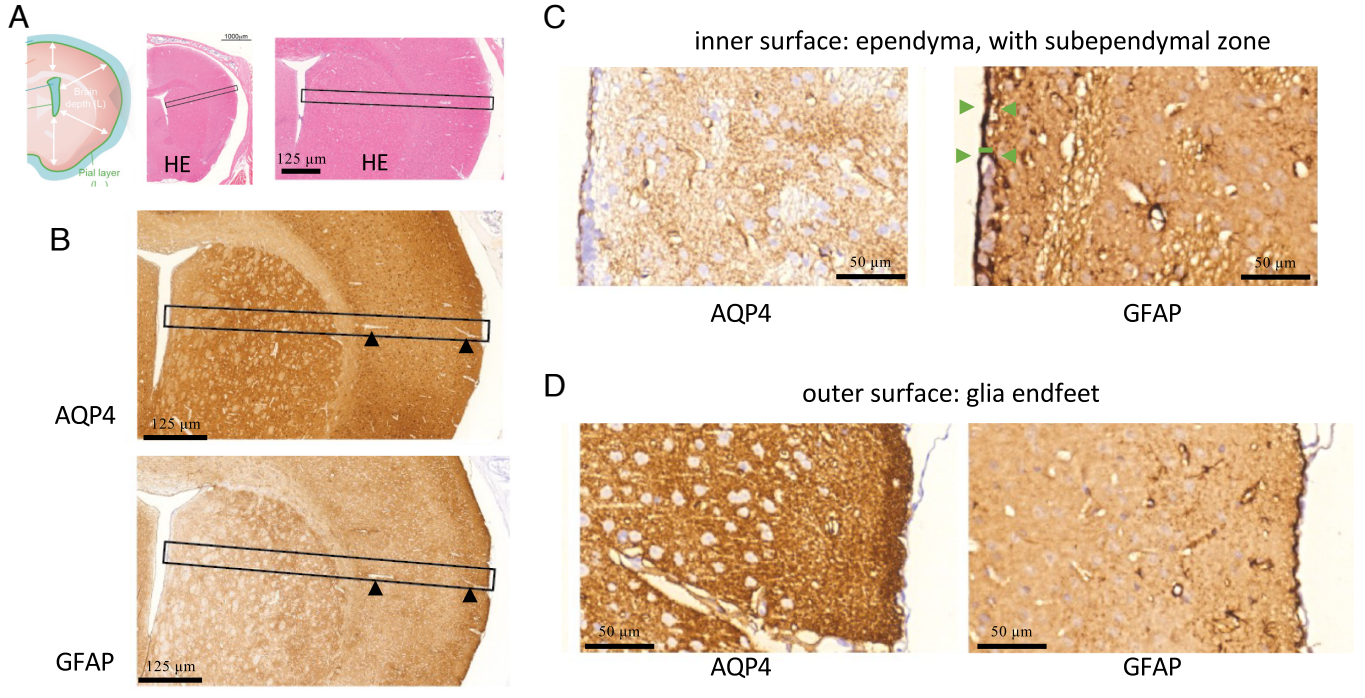

Fig. 5. Histological staining of the coronal section and boundary zones. (*A*) The modeled axis in the coronal section was identified with HE staining of a mouse brain. (*B*) Along the axis from outer to inner surfaces, staining for AQP4 and glia cells (with GFAP) shows gaps for vessels oriented along our hypothesized main direction of transport (arrowheads). (*C*) The ependyma of the inner surface shows attenuated ependymal cells positive for AQP4, with an additional layer corresponding to the stem cell niche revealed by GFAP. The roughly 10 μm layer most strongly stained for GFAP is taken to be the transport bottleneck (green arrowheads and bar). (*D*) The outer surface between the brain and subarachnoid space features a glia limitans zone of AQP4 staining about 25 μm wide, but a much narrower GFAP-positive single cell layer. HE, hematoxylin and eosin; GFAP, glial fibrillary acidic protein; AQP4: aquaporin-4.

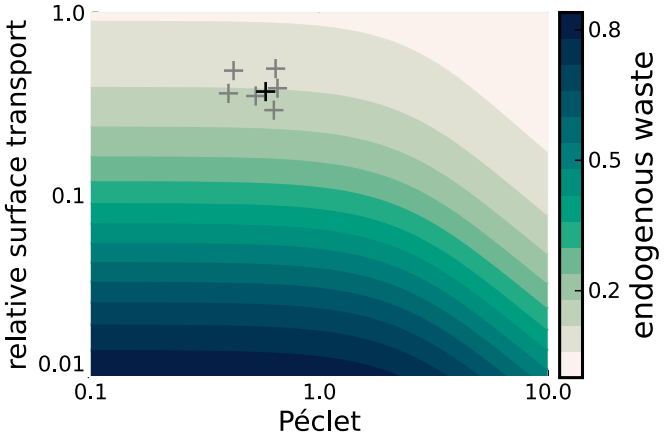

Fig. 6. Steady-state brain content of endogenously produced waste solutes varies considerably with both relative advection (Pe) and surface membrane permeability (γ). In the nondimensionalized model, the total brain content (labeled waste) is a function of three nondimensional parameters, when endogenously produced waste is assumed to rapidly clear from blood and cerebrospinal fluid. One reflects clearance across the blood–brain barrier and we here set that low ($\phi = 0.1$) to investigate clearance when the blood–brain barrier route is ineffective. The remaining two parameters are the Péclet number (Pe) (ratio of advection to diffusion) and γ, which is the relative surface membrane transport. The parameters estimated with MRI from Fig. 4 give $(\mathrm{Pe}, \gamma) = (0.6, 0.4)$ and are shown with a black + while the rest of the MRI datasets are in gray. In this region, stable waste concentrations are somewhat more sensitive to relative surface transport than to advection.

This analysis allows a quantitative and model-based extrapolation to human brain waste clearance. Take a small waste solute like gadobutrol with effective diffusion $D \approx 0.5$ mm/h, similar to the small tracers discussed above, and a distance of 10 mm. Then, the most precise estimate of velocity from above (0.24 mm/h) implies a Péclet number of Pe $\approx$ 5. From this level, increases in advection will cause considerable reductions in brain waste content (along horizontal movement from between Pe = 1.0 and Pe = 10.0 in Fig. 6). Brain waste content falls by 45% when the Péclet number doubles from 5 to 10. Naturally, larger waste products will be more sensitive to advection. For example, 70 kDa peptides (such as immunoglobulins) would have diffusion coefficients smaller by roughly factor $\left(\frac{70}{0.6}\right)^{1/3} \approx 5$ implying Pe = 25. Compared to the small metabolite, bulk flow would cause a larger reduction at 80% of the stable state content. Similarly, increasing the openness of the surface membranes independently lowers brain waste content. This model therefore indicates that bulk flow through tissue can make a considerable contribution to waste clearance and that experimental characterizations of the surface membranes should be a key priority for research in global molecular transport in the brain.

3. Discussion

We have attempted in this study to contain two apparent contradictions in the published brain efflux literature by constructing a simple mathematical model of brain waste accumulation and clearance. A putative restrictive surface membrane layer resolved the contradictions: If the surface layer is efflux rate-limiting, then diffusion within the brain will spread solutes evenly within the brain faster than they can be cleared, leading to the established exponential decay rate even for tracers of varying sizes and in spite of necessary contributions from bulk flow. A short period immediately following tracer infusion in the brain still allows early efflux measurements to accelerate, before settling down to long-run exponential slowing. The model passed testing with two previously published datasets (5, 7). To experimentally validate the model, we developed an assay that allowed minimally invasive real-time imaging of tracer dispersion with improved spatial and temporal resolution. The MRI-based assay had sufficient spatial resolution to estimate the rate-limiting diffusion across the surface membrane. The analysis validated the model, including the proposition that the surface membrane is efflux rate limiting. Finally, when modeling local waste production and clearance, we found that such clearance effectively depends on three nondimensional numbers. One is the relation of bulk flow to diffusion (the Péclet number). Another is the relative clearance across the blood–brain barrier (compared to diffusion within the brain). The final is the ratio of characteristic diffusive speeds across the brain compared to across the surface membrane.

The simplicity of the model allows translation to other studies. To predict patterns of efflux of a given endogenous molecule of interest, other researchers can calculate the corresponding nondimensional numbers for their case, plug the result into Eq. **9** and compare with Fig. 6. In pharmacokinetic studies, the brain and other tissues are often reduced to single compartments and the present model gives quantitative bounds on when such reductions can be justified. A characteristic time-scale for diffusion of solute in the brain is $T = L^2/D$, or 8 h for a small solute at roughly 1 kDa in a brain segment with depth 2 mm, based on our estimates. Due to the rate-limiting boundaries, inert solutes homogenize faster than this within the brain (Movies S1–S3). Therefore, most solutes may be taken to mix well in this brain within a few hours, even when they cannot cross the blood–brain barrier. Since interstitial diffusion is likely faster than transport across surface membranes, efflux on longer time-scales will then essentially be characterized by surface permeability. This goes some way toward explaining why classical studies such as Cserr's (5) found that a single exponential rate could explain efflux of tracers with large size-differences: Their tracers likely all mixed within the brain faster than they were transported out. Our lumped approach may contribute to identifying valid tissue boundary conditions because approaches containing many anatomical and geometrical details instead risk sensitivity to errors in estimates of shape.

Because of the uncertainty about how to interpret brain clearance data, we chose to estimate the entire posterior probability distribution of the estimated model parameters. Compared to the more common point estimates which give only a single number value for parameters, typically due to maximum likelihood estimation or averaging methods, the advantage of estimating the entire posterior probability distribution is particularly clear when this distribution is bimodal. For example, the model interprets the Cserr dataset as implying an average speed of roughly 0.3 mm/h, but is unable to select a preferred direction of flow. The average estimate from this posterior is therefore near 0, and averaged point estimates run the risk of missing that this average holds little probability mass. Maximum likelihood methods would select one of the two modes, but miss the other. To our knowledge, uncertainty quantification of global brain transport has been reported before only by Croci et al. (23). These authors investigated uncertainty in effective diffusion on 3-dimensional gadobutrol transport in the human brain and used a stylized flow field similar to the one-dimensional flow applied here. No formal parameter estimation was conducted, but the authors argue that allowing for uncertainty in diffusion does not obviate the need for a convective flow field to replicate

the experimental results. In our model, the global balance of advection to diffusion with Péclet numbers near 1 suggest that small tracers in the brain will be effluxed both via ventricles and subarachnoid spaces in spite of the unidirectional advection.

Simultaneous estimation of advection and diffusion across the brain are rare in the literature. Modeling of infusion-pump-driven flows is useful for the purpose of the nonphysiological pressures encountered in those situations but has not addressed non-pump-driven flows (27, 28). Theoretical modeling of perivascular pathways as hydraulic networks propose that the volume flow rate is relatively uniform (29, 30), which corresponds to the constant velocity modeled here. Specific estimates of bulk flow velocity range from 0.0, in a report based on extracellular conductivity measured in postmortem neuropil reconstructions (31), to 3.0 mm/h, in a report based on advection–diffusion simulations of small tissue segments containing periarterial and perivenous spaces (32). However, these approaches investigated local rather than global transport and lacked spatial measurements of global transport. Global modeling efforts which have included all three spatial dimensions, but excluded direct estimation of bulk flow, found that diffusive transport would require unrealistically large diffusion parameters to replicate experimental results (33, 34). The study by Valnes et al. (33) highlighted the challenge of correctly modeling boundary conditions, but did not attempt to fit such transport rates directly. Surface effects were also not included in the 3-dimensional advection–diffusion model fitted to human brain data by Vinje et al. (35), but their average velocity range of 0.18 to 0.24 mm/h during sleep is very similar to our results.

Among the limitations of this work is perhaps most importantly the heavily stylized reduction of the geometry to a single dimension forcing the velocity to be a constant average, and the volume-averaging which lumps vascular, perivascular, and interstitial spaces together. Additionally, the assumption of rapid mixing in cerebrospinal fluid is strained since transport from one end of the skull to the other takes nearly half an hour (21). However, blood flow in the capillary bed has been successfully modeled using the homogeneous media assumption (36). This work is therefore well complemented by the larger and more accurate anatomies used in computational models of specific individual brains, which find similar magnitudes of advection (33, 34). In particular, uncertainty quantification of diffusion and advection also indicates in those larger geometries that advection is necessary for accounting for human tracer data (23). Future work could include a spatial dimension for the subarachnoid and ventricle compartments. The permeability of perivascular astrocyte endfoot barriers was recently estimated by Koch et al. (37), and their estimated "diffusion membrane factor" lies between 500 and 6000 m^{-1}. In this work, the comparable number is the relative surface diffusivity D_m/D (≈ 0.01) divided by the membrane length L_m, giving $D_m/D/L_m \approx 10^3$ m^{-1}, in agreement with Koch et al.

Additional limitations include the absence of specified pressure gradients to drive the advective speed and that the model cannot distinguish how much of its average advection is due to perivascular flows versus flows in the interstitium. The averages applied here do not contribute to determining whether the flows are pulsatile or steady. For example, while we chose our prior for the effective diffusion based on data from microscopic experiments done over the course of seconds, dispersive effects due to flow oscillations more rapid than our 5 min MR recording rate would inflate our diffusion estimates (35). Still, based on the work presented here, microscopic (32), macroscopic (34), or lumped-parameter models (30) may be more justified when their average tissue advective speed is in the range 0.08 to 1.5 mm/h. Our parameter estimates should be considered specific to the experimental setups for their respective datasets, including the choice of anesthesia. The Groothuis replications can be used in future validations, but it should be noted that those results confirm the qualitative patterns of the Cserr study, and that disentangling the blood–brain barrier-transport of those tracers from brain surface transport may be statistically difficult.

One remaining question is what the cellular basis is for the surface membranes. It is known that the pial or ependymal membranes covering the brain surfaces and the ventricular walls, respectively, do not form complete coverage and that the cells are loosely connected by gap junctions (38). Thus, it is questionable whether pial or ependymal cells can form membranes that act as size-dependent filters to restrict solute efflux from the brain parenchyma. It is more likely that astrocytic processes physically assemble into the surface barrier. Border-forming glia-limitans astrocytes are positioned directly below the pial and ependymal cells and form a roughly 10 μm layer of heavily interweaved GFAP and AQP4 expressing processes (Fig. 5) (25). The stem cell niche on the lateral anterior horn does not cover the more posterior sections, where transport is thus likely easier. It is interesting to note that the ependyma is more tightly sealed in the fetus than in the adult (39–41). We propose that a key function of glia limitans is to act as a barrier that prevent efflux of extracellular matrix proteins in an analogous function to the collagen-rich membranes that surround peripheral organs. Without a barrier, the extracellular matrix would constantly leak into the surrounding cerebrospinal fluid. For example, hyaluronic acid is abundantly present in the central nervous system and poorly anchored (38). The importance of glia limitans astrocytes is illustrated by the fast formation of new borders by reactive astrocytes that effectively isolate the damaged and inflamed tissue from the surrounding healthy parenchyma (25).

In this study, we synthesized brain clearance assays from mice and rats containing apparent contradictions into a unifying mathematical model, which resolved contradictions with the proposition that a brain surface membrane limits efflux. We then validated the model in a custom in vivo real-time efflux MRI-assay which is the first to measure the necessary spatial tracer transport within and out of brain tissue. The model's nondimensional form enables formal model-based extrapolations and indicates that either the brain surface is relatively permeable to diffusion or bulk flow contributes to clearance of metabolites with low blood–brain barrier permeability.

4. Materials and Methods

4.1. Animals and Drugs. All experiments received approval from Danish Animal Experiments Inspectorate. The C57BL/6J mice (Janvier Labs, Le Genest Saint-Isle, France) were 9 to 14 wk old at the time of the experiment. All animals were group-housed (up to 5 mice/cage) with ad libitum access to food and water, temperature (22 ± 2 °C), and humidity-controlled (55 ± 10%) environment with a 12/12 h light/dark cycle.

4.2. Intrastriatal Cannulations. Intrastriatal cannulations were performed as described by Pla et al. (7). For every animal, the cannulation took place one week before MRI. First, the animals were anesthetized with isoflurane for general anesthesia and injected with lidocaine (1 mg/ml, s.c.) locally at the surgical site, and carprofen (5 mg/kg) and buprenorphine (0.05 mg/kg) subcutaneously for local analgesia. After exposing the skull, a burr hole was drilled in the skull 0.2 mm lateral and 0.6 mm posterior from the bregma, using a dental drill

(Tech2000, RAM Digital Microtorque). Subsequently, an MRI-compatible nylon cannula (0.45 mm outer diameter, Bilaney Consultants, UK) was inserted into the striatum 3.25 mm ventrally from the skull surface and secured using standard dental glue and cement.

4.3. MRI. All mice were put in prone position in the 9.4 T MRI preclinical scanner (BioSpec 94/30 USR, Paravision 6.0.1 software, Bruker BioSpin, Ettlingen Germany). The MRI was performed using room-temperature volumetric Tx/Rx resonator (40-mm inner diameter) and 1,500 mT/m gradient coil (BFG6S, Bruker), in mice anesthetized with a mixture of ketamine (75 mg/kg) and dexmedetomidine (1 mg/kg). An MR-compatible remote monitoring system (SA Instruments, NY, USA) was used to maintain body temperature at 37 ± 0.5 Celsius with a thermostatically controlled waterbed along with monitoring of respiratory rate. The protocol consisted of T2-weighted 3D-CISS morphological reference acquired with 100 μm isotropic spatial resolution (TR/TE 4/2 ms, Nex 1, FA 50°, FOV 19.2 × 19.2 × 16 mm, Matrix 192 × 192 × 160, maximum intensity projection of 4 orthogonal phase encoding directions), and subsequent DCE-MRI with a T1W-3D-fast low angle shot (3D-FLASH) sequence (TR/TE 7.1/1.5 ms, FA 10°, FOV 19.2 × 19.2 × 16mm, Matrix 192 × 192 × 160). Each 3D-FLASH volume was acquired in 6 min, and T1-enhancing contrast agent gadobutrol (20 mM; Gadovist, Bayer Pharma AG, Leverkusen, Germany) was infused into the striatum (0.1 μL/min for 10 min, total infusion volume = 1 μL) after the first 3 baseline 3D-FLASH volumes acquired (i.e., 18 min). The scanning continued over 20 measurements (120 min).

4.4. Image Processing. All 3D-CISS volumes were calculated in few steps using in-house preprocessing pipeline. For each animal, both 3D-TrueFISP volumes acquired with four orthogonal phase encoding directions and DCE FLASH volumes were motion-corrected and spatially normalized with Advanced Normalization Tools (ANTs) (reference: B. B. Avants et al., A reproducible evaluation of ANTs similarity metric performance in brain image registration. Neuroimage 54, 2033–2044 (2011). doi: https://doi.org/10.1016/j.neuroimage.2010.09.025; pmid: 20851191). Motion-corrected 3D-CISS image was computed as a maximum intensity projection, resulting in an image of almost completely removed banding artifacts. DCE FLASH volumes were then coregistered to the 3D-CISS volumes. To normalize the CSF signal in each time series, their voxel intensities were subjected to Gaussian normalization using the first 3D-FISP volume. The resulting images were smoothed with a 3 × 3 × 3 voxels kernel of [0.2, 1, 0.2] weights for along each axis, to reduce the influence of possible artifacts after automatic affine registration and subtraction of the baseline volume.

4.5. Histology. Complete series of serial paraffin sections of the entire forebrain of C57BL/6J mice were available from a previous study (42). For ordinary histology and immunocytochemistry, coronal sections from the relevant region were processed according to standard protocols (see ref. 42) and incubated overnight at 4 °C with the anti-AQP4 primary antibody AVIVA Systems Biology (OABB01958); 1:3000 following antigen retrieval in citrate buffer, pH 6 and the anti-GFA-P primary antibody Dako (Z0334); 1:10000 following antigen retrieval in TEG buffer, pH 9. diluted in 10% goat serum and washed with TBS. For bright field light microscopy analysis, the REALTM EnVisionTM Detection System, Peroxidase/Diaminobenzidine+ (DAB+) rabbit/mouse, (K5007, Dako, Glostrup, Denmark) was used for detecting the primary antibodies. The detection reagent consists of a dextran backbone coupled to peroxidase and polyclonal secondary antibody molecules. The sections were washed with TBS, followed by incubation for 10 min with the DAB+ solution. Sections were counterstained with Mayer's hematoxylin, dehydrated in graded alcohols, and cover-slipped with Pertex mounting medium.

4.6. Global Glymphatic Model. The application of the advection–diffusion equation with first-order reaction kinetics for blood–brain barrier transport has been previously described (8). In brief, we average solute concentrations c in the brain over small volumes containing 20% extracellular space taken to be homogeneous media through which solute is transported with effective diffusion coefficient D and superficial velocity v. The effective diffusion coefficient depends on tortuosity and extracellular space volume fraction (9), but we do not attempt to resolve this relationship for this work. Brain tissue is three-dimensional, but perivascular spaces penetrate at right angles to the brain surface and since these may be the main solute highways, we consider only transport along the axis in the radial direction of these channels which are roughly the shortest, straight lines between subarachnoid spaces and ventricles. Originally, we used a spherical geometry for the brain with an inner sphere representing ventricles. This emphasized our assumption that solute transport is on average symmetrical on the plane orthogonal to penetrating perivascular spaces. However, the ratio of ventricular surface area to superficial surface area required by a spherical model seems a distortion of the relatively large ventricular areas. We therefore moved to a slab geometry in which the four sides of the three-dimensional cuboid parallel to the main axis have symmetrical boundary conditions, resulting in our formulation of the advection–diffusion equation on a straight line between ventricle and subarachnoid space (Fig. 2 and Eq. **2a**).

The tissue boundaries require special attention, something which we find has been lacking in existing modeling (though see ref. 43). It is currently unknown how permeable the surface membranes are. We chose to let a fraction r_e of the surfaces be a single-cell layer, in which we assume pure Fick's diffusive flux J_m, and a fraction $1 - r_e$ to be open fluid space, in which advection and diffusion combines in the flux J_p. Since these surface layers are narrow, we can assume a rapid steady-state concentration profile with Dirichlet boundary conditions and calculate the resulting combined flux over such a membrane and open space, $J = r_e J_m + (1 - r_e) J_p$. To satisfy mass conservation, this surface flux must equal the flux on the border of the tissue, $vc - D\frac{\partial}{\partial l}c = J$. We therefore get Robin boundary conditions for the advection–diffusion–reaction Eq. **2b**–**2c**. Since r_e is challenging to separate from D_m in parameter identification from data, we limit the investigations here to the case $r_e = 1$, corresponding to complete coverage of the surface cell layer. The steady-state concentration in a narrow layer of diffusion with Dirichlet boundary conditions is linear, so the flux through it is everywhere

$$J_m(l) = J_m = \alpha \frac{D_m}{L_m} \Delta c, \qquad [1]$$

where Δc is the difference between extracellular concentration c/α and external concentration c_c or c_v, and α is the extracellular volume fraction of the tissue. This is because the membrane flux occurs only through the surface not occluded by cells (neurons, astrocytes) and due to a concentration difference which scales the flux.

As with earlier models, we assume that the blood–brain barrier is homogeneously distributed in tissue and use first-order solute exchange with the blood compartment, in which the solute concentration is c_b, with rate k_p (8). We add a production term p to investigate the effect of diffusion and advection of locally produced waste products, as has been done before (8). This completes the formulation of the central advection–diffusion–reaction model, Eqs. **2a**–**2c**.

$$\frac{\partial}{\partial t}c(l,t) = D\frac{\partial^2}{\partial l^2}c(l,t) - v\frac{\partial}{\partial l}c(l,t) + p - k_p[c(l,t) - c_b(t)], \qquad [2a]$$

$$\frac{\partial}{\partial l}c(0,t) = D^{-1}[vc(0,t) - r_e J_m(0) + (1 - r_e)J_p(0)], \qquad [2b]$$

$$\frac{\partial}{\partial l}c(L,t) = D^{-1}[vc(L,t) - r_e J_m(L) + (1 - r_e)J_p(L)]. \qquad [2c]$$

The two tissue surfaces interact with rapidly mixed solute in cerebrospinal fluid in ventricles (subscript v) with concentration c_v and in subarachnoid spaces (subscript c) with concentration c_c. The net production of cerebrospinal fluid also sets the net volume throughput from ventricles to subarachnoid spaces and onward to blood, Q_l, (via unspecified efflux routes). A small backflow from subarachnoid space to ventricles, Q_r, is included. Given the surface area S we can now calculate in- and efflux of solute mass m to these control volumes, and with V_c and V_v being the subarachnoid space and ventricular volumes respectively, we also have their concentrations. This parameterization with a single surface area S requires the whole brain slab to have similar tracer concentrations at a given depth l. Last, the control volume for blood (subscript b) receives exactly the mass crossing the blood–brain barrier and from the subarachnoid space. This

completes the state space of the model Eqs. **2**–**5**, which conserves mass (which accumulates in blood).

$$\frac{\partial}{\partial t}m_v = V_v\frac{\partial}{\partial t}c_v = -SJ(0) - Q_l c_v - Q_r(c_v - c_c), \quad [3]$$

$$\frac{\partial}{\partial t}m_c = V_c\frac{\partial}{\partial t}c_c = SJ(L) - Q_l c_c + Q_r(c_v - c_c), \quad [4]$$

$$\frac{\partial}{\partial t}m_b = V_b\frac{\partial}{\partial t}c_b = S\int_0^L k_p[c(l,t) - c_b(t)]\mathrm{d}l + Q_l c_c. \quad [5]$$

To solve the system, we implemented a numerical solution scheme in Julia (44) using DifferentialEquations.jl (45) and checked that all simulations respected total mass conservation (*SI Appendix*, Fig. S11).

To get a nondimensionalized model and find nondimensional parameter groups, we scaled lengths with L, time with L^2/D, and concentrations by p/k_p. This allows rephrasing the model for the brain domain along the axis ℓ over time τ with nondimensional concentrations C and nondimensional parameter groups $\mathrm{Pe} = vL/D$, $\phi = k_p L^2/D$, and $\gamma = \alpha\frac{D_m}{L_m}/\frac{D}{L}$:

$$\frac{\partial}{\partial\tau}C = \frac{\partial^2}{\partial\ell^2}C - \mathrm{Pe}\,\frac{\partial}{\partial\ell}C + \phi(1 + C_b - C), \quad [6]$$

$$\frac{\partial}{\partial\ell}C(0,\tau) = \mathrm{Pe}\;C(0,\tau) - \gamma\,(C_v - C(0,\tau)), \quad [7]$$

$$\frac{\partial}{\partial\ell}C(1,\tau) = \mathrm{Pe}\;C(1,\tau) - \gamma\,(C(1,\tau) - C_c). \quad [8]$$

The steady-state situation, where $\frac{\partial}{\partial\tau}C = 0$, is then a second-order inhomogeneous differential equation if solute is rapidly cleared from cerebrospinal fluid and blood ($C_v = C_c = C_b = 0$). This problem was solved using Maple (version 2020.1) to give the analytical solution in Eq. **9**.

$$C = 1 - \frac{\mathrm{e}^{ax}\left(\mathrm{e}^b\mathrm{Pe}C + C\,\mathrm{e}^b\gamma + \mathrm{e}^b\mathrm{Pe}^2 - \mathrm{e}^b\mathrm{Pe}\gamma - 2\,\mathrm{e}^b\gamma^2 - C\mathrm{Pe} + C\gamma - \mathrm{Pe}^2 - \mathrm{Pe}\gamma + 2\gamma^2\right)}{2C\,\mathrm{e}^b\gamma + 2\,\mathrm{e}^a C\gamma - 2\,\mathrm{e}^b\gamma^2 + 2\,\mathrm{e}^a\gamma^2 - 2\,\mathrm{e}^b\phi + 2\,\mathrm{e}^a\phi}$$
$$- \frac{2\,\mathrm{e}^{bx}\left(\mathrm{e}^a C\mathrm{Pe}\gamma + \mathrm{e}^a C\gamma^2 + \mathrm{e}^a\mathrm{Pe}\gamma^2 + \mathrm{e}^a\gamma^3 + \mathrm{e}^a\mathrm{Pe}\phi + \mathrm{e}^a\phi\gamma + \mathrm{Pe}^2\gamma - \gamma^3 - \mathrm{Pe}\phi + \phi\gamma\right)}{(\mathrm{Pe} + 2\gamma + C)\left(C\,\mathrm{e}^b\gamma + \mathrm{e}^a C\gamma - \mathrm{e}^b\gamma^2 + \mathrm{e}^a\gamma^2 - \mathrm{e}^b\phi + \mathrm{e}^a\phi\right)}. \quad [9]$$

For this equation, we used the simplifications $a = (\mathrm{Pe} + \sqrt{\mathrm{Pe} + 4\phi})/2$ and $b = (\mathrm{Pe} - \sqrt{\mathrm{Pe} + 4\phi})/2$ to reduce the expression. By integrating the solution over the brain domain, we find the total brain content of the (nondimensional) solute as a function of Pe, ϕ, and γ. Notice that the scaling of concentrations with p/k_p results in waste concentration scaled such that local steady state with respect to blood–brain barrier efflux has (nondimensional) concentration 1.

4.7. Measurement Model, Priors, and Posterior Estimation. Our approach to estimating the posteriors follows that of Gelman et al. (46). We expect measurements y to be correct on average, but due to measurement and model errors, the experimental observations will be distributed around the model predictions $\hat{y}$. We take the error distribution to be normal $\mathcal{N}(\hat{y}, \sigma_m^2)$, with an error σ_m about which we only know that it will be less than some $\overline{o_m}$, learned from the particular measurement set m, so that $\overline{o_m}$ has a uniform prior distribution $\mathcal{U}(0, \overline{o_m})$. With the errors taken to be independent, we can now formalize the probability of making a particular set of observations $y_m(l, t_j)$, where m refers to the measurement variable, j counts the J measurement time-points and l is the initial condition. Let $y(l,t)$ be all the measurements for brevity and let σ^2 represent all noise terms. The model predictions $\hat{y}$ likewise depend on initial condition l and time t, but also our parameters. In sum, we assume that the measurements are normally distributed around the model predictions:

$$\Pr\left(y(l,t)|\hat{y}(l,t,D,D_m,v),\sigma^2\right) = \prod_{m=1}^{M}\prod_{j=1}^{J}\mathcal{N}\left(\hat{y}(l,t_j,D,D_m,v),\sigma_m^2\right), \quad [10]$$

where $\hat{y}$ solves the model Eqs. **2**–**5**. We note that this approach models prediction errors as arising from measurement noise rather than model error.

4.7.1. Setting cautious priors. Our prior hypotheses on the D, D_m, and v parameters vary considerably. Strong priors are set on D, which have a thorough history of theoretical and empirical investigations (9). We calculate the median effective diffusion constants μ_D by correcting the Stokes–Einstein pure diffusion estimate, D_{SE}, for tortuosity $\lambda = 1.7$, to get $\mu_D = D_{\mathrm{SE}}/\lambda^2$ (22). We take the log of the true effective diffusion constant to be normally distributed around $\log\mu_D$ with its prior variance $\tau_D^2 = 0.5^2$, set to roughly fit the reported variance in measurements of λ (9)*: $\log D \sim \mathcal{N}(\log\mu_D, \tau_D^2)$. We use conservative priors on the advective velocity v, since its magnitude is debated. With its mean on 0 mm/h and a variance of $\tau_v = 1$ mm/h, 99% of the probability mass for v is smaller than the upper limit estimated by Ray et al. (50 μm/min = 3 mm/h) (32) and we are agnostic about the direction of flow before learning from the data. Finally, the diffusion through the tissue surface membrane, D_m, has little prior information: It may be similar to that of the tissue itself ($D_m \approx D$), or these cells could reasonably make D_m 100 times smaller ($D_m \approx 10^{-2}D$). For this reason, we use a uniform prior on D_m, allowing it to be between 0 and $\overline{D_m} = 1\ \mathrm{mm}^2/\mathrm{h} \approx 2D$, so $D_m \sim \mathcal{U}(0, \overline{D_m})$. The parameters for uncertainty quantification are summarized in Table 2.

Two notes on these priors: We do not represent population variation in the parameters, and assume constant velocity throughout the experimental time-periods. Estimating population variation is possible in our chosen data sources with multiple animals, but since their mean measurements were found to be representative, we chose to limit this analysis accordingly. Variation in average advective velocity is quite possible in especially experiments of long duration (e.g., 30 h in Cserr et al.), but again we restrict this analysis to the case of constant velocity.

To summarize, our independent priors are

$$\sigma_m^2 \sim \mathcal{U}(0.0, \overline{o_m})$$
$$\log D \sim \mathcal{N}(\log\mu_D, \tau_D^2)$$
$$D_m \sim \mathcal{U}(0, \overline{D_m})$$
$$v \sim \mathcal{N}(0, \tau_v^2).$$

Table 2. Parameters for uncertainty quantification and Bayesian parameter estimation

Parameter	Dataset	Value	Units
τ_v	all	1.0	mm/h
μ_D	all	0.46	mm^2/s
τ_D	all	0.5	1
$\overline{D_m}$	all	1.0	mm^2/h
$\overline{o_{\mathrm{bm}}}$	Pla	1.0	μg
$\overline{o_{\mathrm{bl}}}$	Pla	0.01	μg/mL
$\overline{o_{\mathrm{bm}}}$	Cserr	20.0	% infused mass
$\overline{o_c}$	Cserr	4.0	% infused mass

*We silently drop the units through the log-transformation.

4.7.2. Estimation of the posterior. The product of our likelihood and our prior gives the joint posterior probability distribution for our parameters of interest D, D_m, and v, as well as our observation deviation σ^2. The denominator is constant and sampling the numerator is therefore sufficient. We sample the numerator with the No U-Turn Sampler provided in the Turing library (with standard acceptance rate 0.65) which normalizes out the denominator and converges to the posterior distribution (47); see Eq. **11**. The second equality follows from our assumption of independence between the parameters and measurement variance. The proportionality follows from the denominator being constant, and we have used $\Pr(\sigma_m^2) = \overline{o_m}^{-1}$ (and avoided subscripts on σ^2 when not indexing over measurement method). Due to numerical instability issues with very small and very large values of D, we truncate the priors D to $[0.01, 20]$ mm^2/h and v to $[-2, 2]$ mm/h and examine the posterior chains (*SI Appendix*, Figs. S12 and S22) to check the quality of posterior sampling.

$$\begin{aligned}\Pr(D, D_m, v, \sigma^2 \mid y, I, t, \bar{o}_m, \tau_D^2, \overline{D_m}, \tau_v^2) &= \frac{\Pr(y \mid t, I, D, D_m, v, \sigma^2)\Pr(D, D_m, v, \sigma_m^2 \mid \bar{o}_m, \tau_D^2, \overline{D_m}, \tau_v^2)}{\Pr(y)} \\ &= \frac{\Pr(y \mid t, I, D, D_m, v, \sigma^2)\Pr(D|\mu_D, \tau_D^2)\Pr(D_m|\overline{D_m})\Pr(v|\tau_v^2)\Pr(\sigma^2, \mid \overline{o_m}))}{\Pr(y)} \\ &\propto \left(\prod_{m=1}^{M}\prod_{j=1}^{J}\mathcal{N}(\hat{y}_m(I, t_j, \theta, D, D_m, v), \sigma_m^2)\right)\prod_{m=1}^{M}\overline{o_m}^{-1} \\ &\quad \times \left(\mathcal{N}(\log \mu_D, \tau_D^2)\,\mathcal{U}(0, \overline{D_m})\,\mathcal{N}(0, \tau_v^2).\right) \qquad [11]\end{aligned}$$

4.7.3. Parameter robustness analysis. To examine to what extent the results are sensitive to the nine physiological constants (Table 1), we simultaneously replaced each with a normal distribution centered on its expected value with a SD at 10% of this value and truncated by factor 10 below and above. Performing the posterior sampling in otherwise the same way as above, we found that this procedure allows the model a qualitatively better fit to the data, see the accompanying code repository.

4.7.4. Data parsing, implementation, and other notes. All code necessary to replicate these results is publicly available in ref. 48, in the form of a Julia package using in particular the DifferentialEquations.jl and Turing.jl libraries (44, 45, 47).

In order to set the initial condition for the model simulations, we took the initial concentration profile from the measurements by Pla (7). From the several Pla recordings, we chose the median.

We assumed the volume of cerebrospinal fluid, V_c, to be roughly evenly split between ventricles and the remaining subarachnoid space. Model predictions on concentration profiles are not very sensitive to this parameter (analyses not presented here).

Data, Materials, and Software Availability. Code and MRI profiles data have been deposited in Zenodo (https://doi.org/10.5281/zenodo.10582168) (49).

ACKNOWLEDGMENTS. We thank Dan Xue for contributions to figure design and Pernille S. Froh for excellent help with the histology.

1. V. M. Savage, G. B. West, A quantitative, theoretical framework for understanding mammalian sleep. *Proc. Natl. Acad. Sci. U.S.A.* **104**, 1051–1056 (2007).
2. J. Cao, A. B. Herman, G. B. West, G. Poe, V. M. Savage, Unraveling why we sleep: Quantitative analysis reveals abrupt transition from neural reorganization to repair in early development. *Sci. Adv.* **6**, eaba0398 (2020).
3. L. Xie *et al.*, Sleep drives metabolite clearance from the adult brain. *Science* **342**, 373–377 (2013).
4. J. H. Thomas, Theoretical analysis of wake/sleep changes in brain solute transport suggests a flow of interstitial fluid. *Fluid. Barr. CNS* **19**, 1–5 (2022).
5. H. Cserr, D. Cooper, P. Suri, C. Patlak, Efflux of radiolabeled polyethylene glycols and albumin from rat brain. *Am. J. Physiol.-Renal Physiol.* **240**, F319–F328 (1981).
6. D. R. Groothuis *et al.*, Efflux of drugs and solutes from brain: The interactive roles of diffusional transcapillary transport, bulk flow and capillary transporters. *J. Cereb. Blood Flow Metab.* **27**, 43–56 (2007).
7. V. Pla *et al.*, A real-time in vivo clearance assay for quantification of glymphatic efflux. *Cell Rep.* **40** (2022).
8. C. Nicholson, Diffusion and related transport mechanisms in brain tissue. *Rep. Progr. Phys.* **64** (2001).
9. E. Syková, C. Nicholson, Diffusion in brain extracellular space. *Physiol. Rev.* **88**, 1277–1340 (2008).
10. Aifb science, Allen mouse brain atlas [p56, coronal] (2011).
11. L. Swanson, *Brain Maps: Structure of the Rat Brain* (Elsevier Academic Press, 2004).
12. P. Blinder, A. Y. Shih, C. Rafie, D. Kleinfeld, Topological basis for the robust distribution of blood to rodent neocortex. *Proc. Natl. Acad. Sci. U.S.A.* **107**, 12670–12675 (2010).
13. A. J. Jiménez, M. D. Domínguez-Pinos, M. M. Guerra, P. Fernández-Llebrez, J. M. Pérez-Fígares, Structure and function of the ependymal barrier and diseases associated with ependyma disruption. *Tissue Barr.* **2**, e28426 (2014).
14. E. Van Vliet, W. Otte, J. Gorter, R. Dijkhuizen, W. Wadman, Longitudinal assessment of blood-brain barrier leakage during epileptogenesis in rats. a quantitative MRI study. *Neurobiol. Diseas.* **63**, 74–84 (2014).
15. R. Rudick, D. Zirretta, R. Herndon, Clearance of albumin from mouse subarachnoid space: A measure of CSF bulk flow. *J. Neurosci. Methods* **6**, 253–259 (1982).
16. N. Kaliss, D. Pressman, Plasma and blood volumes of mouse organs, as determined with radioactive iodoproteins. *Proc. Soc. Expe. Biol. Med.* **75**, 16–20 (1950).
17. L. Wang, Plasma volume, cell volume, total blood volume and fcells factor in the normal and splenectomized sherman rat. *Am. J. Physiol.-Legacy Content* **196**, 188–192 (1958).
18. H. B. Lee, M. D. Blaufox, Blood volume in the rat. *J. Nuclear Med.* **26**, 72–76 (1985).
19. G. Liu *et al.*, Direct measurement of cerebrospinal fluid production in mice. *Cell Rep.* **33**, 108524 (2020).
20. R. O. Tuura, C. Volk, F. Callaghan, V. Jaramillo, R. Huber, Sleep-related and diurnal effects on brain diffusivity and cerebrospinal fluid flow. *NeuroImage* **241**, 118420 (2021).
21. E. H. Stanton *et al.*, Mapping of CSF transport using high spatiotemporal resolution dynamic contrast-enhanced MRI in mice: Effect of anesthesia. *Magnet. Reson. Med.* **85**, 3326–3342 (2021).
22. C. Nicholson, S. Hrabětová, Brain extracellular space: The final frontier of neuroscience. *Biophys. J.* **113**, 2133–2142 (2017).
23. M. Croci, V. Vinje, M. E. Rognes, Uncertainty quantification of parenchymal tracer distribution using random diffusion and convective velocity fields. *Fluids Barr. CNS* **16**, 1–21 (2019).
24. C. B. Brochner, C. B. Holst, K. Mollgard, Outer brain barriers in rat and human development. *Front. Neurosci.* **9**, 75 (2015). C. B. Brochner, C. B. Holst, C. B. Mollgard, Kjeld eng Switzerland 2015/04/09 *Front. Neurosci.* **9**, 75 (2015). 10.3389/fnins.2015.00075.eCollection.
25. M. V. Sofroniew, Astrocyte barriers to neurotoxic inflammation. *Nat. Rev. Neurosci.* **16**, 249–263 (2015).
26. P. Hasel *et al.*, Defining the molecular identity and morphology of glia limitans superficialis astrocytes in mouse and human. bioRxiv [Preprint] (2023). https://pubmed.ncbi.nlm.nih.gov/37066303/ (Accessed 5 June 2023).
27. K. H. Støverud, M. Darcis, R. Helmig, S. M. Hassanizadeh, Modeling concentration distribution and deformation during convection-enhanced drug delivery into brain tissue. *Trans. Porous Med.* **92**, 119–143 (2012).
28. J. J. García, J. H. Smith, A biphasic hyperelastic model for the analysis of fluid and mass transport in brain tissue. *Ann. Biomed. Eng.* **37**, 375–386 (2009).
29. M. X. Wang, L. Ray, K. F. Tanaka, J. J. Iliff, J. Heys, Varying perivascular astroglial endfoot dimensions along the vascular tree maintain perivascular-interstitial flux through the cortical mantle. *Glia* **69**, 715–728 (2021). M. X. Wang, L. Ray, K. F. Tanaka, J. J. Iliff, J. Heys,, Jeffrey eng R01 AG054456/AG/NIA NIH HHS/ R01 NS089709/NS/NINDS NIH HHS/ Research Support, N.I.H., Extramural 2020/10/20 Glia. 2021 Mar;69(3):715-728. 10.1002/glia.23923. Epub 2020 Oct 19.
30. J. Tithof *et al.*, A network model of glymphatic flow under different experimentally-motivated parametric scenarios. *iScience* **25**, 104258 (2022).
31. K. E. Holter *et al.*, Interstitial solute transport in 3D reconstructed neuropil occurs by diffusion rather than bulk flow. *Proc. Natl. Acad. Sci. U.S.A.* **114**, 9894 (2017).
32. L. Ray, J. J. Iliff, J. J. Heys, Analysis of convective and diffusive transport in the brain interstitium. *Fluids Barr. CNS* **16** (2019).
33. L. M. Valnes *et al.*, Apparent diffusion coefficient estimates based on 24 hours tracer movement support glymphatic transport in human cerebral cortex. *Sci. Rep.* **10** (2020).
34. L. A. Ray, M. Pike, M. Simon, J. J. Iliff, J. J. Heys, Quantitative analysis of macroscopic solute transport in the murine brain. *Fluids Barr. CNS* **18**, 55 (2021).
35. V. Vinje *et al.*, Human brain solute transport quantified by glymphatic MRI-informed biophysics during sleep and sleep deprivation. *Fluids Barr. CNS* **20**, 62 (2023).

36. Y. Qi, M. Roper, Control of low flow regions in the cortical vasculature determines optimal arterio-venous ratios. *Proc. Natl. Acad. Sci. U.S.A.* **118** (2021).
37. T. Koch, V. Vinje, K. A. Mardal, Estimates of the permeability of extra-cellular pathways through the astrocyte endfoot sheath. *Fluid. Barriers CNS* **20**, 20 (2023). T. Koch, V. Vinje, K. A. Mardal, eng 801133/Horizon 2020 Framework Programme/ England 2023/03/22 Fluids Barriers CNS. 2023 Mar 20;20(1):20. 10.1186/s12987-023-00421-8.
38. M. K. Rasmussen, H. Mestre, M. Nedergaard, Fluid transport in the brain. *Physiol. Rev.* **102**, 1025–1151 (2022).
39. N. R. Saunders, K. M. Dziegielewska, K. Mollgard, M. D. Habgood, Physiology and molecular biology of barrier mechanisms in the fetal and neonatal brain. *J. Physiol.* **596**, 5723–5756 (2018). N. R. Saunders, K. M. Dziegielewska, K. Mollgard, M. D. Habgood, eng Wellcome Trust/United Kingdom Review England 2018/05/19 *J. Physiol.* **596**, 5723–5756 (2018). 10.1113/JP275376. Epub 2018 Jul 15.
40. Y. Balslev, N. R. Saunders, K. Mollgard, Ontogenetic development of diffusional restriction to protein at the pial surface of the rat brain: An electron microscopical study. *J. Neurocytol.* **26**, 133–148 (1997). Y. Balslev, N. R. Saunders, K. Mollgard, Research Support, Non-U.S. Gov't 1997/03/01 *J. Neurocytol.* **26**, 133–148 (1997). 10.1023/a:1018527928760.
41. K. Mollgard, Y. Balslev, B. Lauritzen, N. R. Saunders, Cell junctions and membrane specializations in the ventricular zone (germinal matrix) of the developing sheep brain: A CSF-brain barrier. *J. Neurocytol.* **16**, 433–44 (1987). K. Mollgard, Y. Balslev, B. Lauritzen, N. R. Saunders, Research Support, Non-U.S. Gov't 1987/08/01 *J. Neurocytol.* **16**, 433–444 (1987). 10.1007/BF01668498.
42. K. Mollgard *et al*., A mesothelium divides the subarachnoid space into functional compartments. *Science* **379**, 84–88 (2023). K. Mollgard *et al*., 2023/01/06 *Science* **379**, 84–88 (2023). 10.1126/science.adc8810. Epub 2023 Jan 5.
43. A. D. Martinac, D. F. Fletcher, L. E. Bilston, Phase offset between arterial pulsations and subarachnoid space pressure fluctuations are unlikely to drive periarterial cerebrospinal fluid flow. *Biomech. Model. Mechanobiol.* **20**, 1751–1766 (2021).
44. J. Bezanson, A. Edelman, S. Karpinski, V. B. Shah, Julia: A fresh approach to numerical computing. *SIAM Rev.* **59**, 65–98 (2017).
45. C. Rackauckas, Q. Nie, Differentialequations.jl-A performant and feature-rich ecosystem for solving differential equations in Julia. *J. Open Res. Softw.* **5** (2017).
46. A. Gelman *et al*., *Bayesian Data Analysis* (2021), vol. 3.
47. H. Ge, K. Xu, Z. Ghahramani, "Turing: A language for flexible probabilistic inference" in *International Conference on Artificial Intelligence and Statistics* (PMLR, 2018), pp. 1682–1690.
48. PAR Bork, Glymphatics1d-pnas2024, Zenodo. https://zenodo.org/doi/10.5281/zenodo.10582168. Accessed 29 January 2024.
49. P. A. R. Bork, Glymphatics1D-PNAS2024. Zenodo. https://doi.org/10.5281/zenodo.10582168. Deposited 29 January 2024.